Int J Adv Manuf Technol (2017) 93:2215–2226
DOI 10.1007/s00170-017-0691-5

ORIGINAL ARTICLE

Simulating welding residual stress and deformation in a multi-pass butt-welded joint considering balance between computing time and prediction accuracy

Xiaowei Pu[1] · **Chaohua Zhang**[1] · **Suo Li**[1] · **Dean Deng**[1]

Received: 18 March 2017 / Accepted: 14 June 2017 / Published online: 29 June 2017

Abstract In this study, three different modeling approaches, namely, a model with moving heat source, a model with high effective heat source named instantaneous heat source, and a model with instantaneous heat source as well as coarser mesh density, were employed to systematically investigate welding residual stress and deformation in a multi-pass butt-welded joint. Moreover, the difference of material properties especially yield stress between base metal and weld has been considered. In addition, the hole-drilling method and three-coordinate measuring technique were employed to obtain welding residual stress distribution and deformation, respectively. The comparison between simulation results and measurements suggests that the model with moving heat source can obtain a good prediction of both welding residual stress and deformation, while the model with instantaneous heat source can only provide a reasonable result for welding residual stress but fail to predict welding deformation. However, the latter model can save a large amount of computing time. Numerical results indicate that the mesh density in the longitudinal direction has an insignificant influence on the calculated results of welding residual stress and deformation if the developed instantaneous heat source model has been used. From the viewpoint of engineering application, the model with instantaneous heat source model and coarser mesh density is potentially able to predict welding residual stress distribution in thick-plate joint using a shorter computing time.

Keywords Welding deformation · Residual stress · Finite element method · Computing time · Prediction accuracy

✉ Dean Deng
deandeng@cqu.edu.cn

[1] College of Materials Science and Engineering, Chongqing University, Shazheng Street 174, Shapingba, Chongqing 400044, China

1 Introduction

Arc welding is one of the most commonly joining techniques used in many manufacturing industries such as steel structure construction, power plant, ship building, and so on, due to its high productivity, design flexibility, and cost effectiveness. Owing to the highly concentrated heat input used in the welded joint, residual stress especially the high tensile residual stress and deformation are developed in and around the weld region due to the large temperature gradients generated among the weld, heat-affected zone, and base metal. The exaggerated welding residual stress in the weld zone and its vicinity seriously affect ultimate strength, fatigue strength, and structural stability. In addition, excessive deformation in welded structures significantly degrades manufacturing accuracy. Therefore, an accurate and reliable prediction of the welding residual stress and deformation is very important [1].

With the rapid development of the computational welding mechanics and the computer technology, computational approaches based on the finite element method have been improved stepwise and widely used to predict the welding residual stress and deformation in actual engineering structures [2, 3]. However, one of the larger obstacles which postpone the application of numerical welding simulation in virtual manufacturing industries is the too long calculated time if the dimensions of the weld part are too large. Therefore, to develop highly effective and accurate computation tools is an urgent, meaningful, and challenging task in welding community [4].

Up to now, several simplified methods to predict welding residual stress and deformation have been proposed to increase computing speed [5–10]. Based on the moving heat source with

Gauss distribution, Cai and his co-workers [11] established a simplified heat source named string heat source model to shorten computing time. Hong et al. [12] proposed a method to combine several weld passes into an equivalent one. Although this method can largely reduce the total number of weld pass in numerical model, it just can roughly estimate the welding residual stress and the computational accuracy cannot be guaranteed. Recently, Murakawa and his co-workers [13, 14] developed an iterative substructure method based on their in-house program to significantly accelerate computing speed in 3D finite element analyses. Deng and Kiyoshima [15] proposed a heat source model named variable length heat source to simulate welding residual stress distribution in a multi-pass butt-welded joint for saving computing time and keeping a highly accurate prediction. Barsoum et al. [16] proposed a computational approach with rapid dumping to simplify the heat source model so as to shorten the computing time. Most recently, Ma [17] developed an accelerated explicit method and graphical processing units parallel computing program to simulate welding-induced transient thermal stress and deformation for large-scale welded structures.

When a commercial software such as MSC. Marc is adopted to predict welding residual stress distribution and deformation in a multi-pass welded joint, the computing time and prediction accuracy can be balanced through carefully considering modeling approach. In a modeling approach, the computing time can be largely reduced through employing a simplified heat source model and designing a reasonable mesh. This consideration is very meaningful to analyze the welding residual stress distribution and deformation for the practical engineering welded structures.

In the current study, both numerical simulation technology and experimental method were employed to obtain the welding residual stress distribution and deformation for validation. Firstly, three finite element models, namely, a model with moving heat source, a model with instantaneous heat source, and a model with instantaneous heat source as well as coarser mesh density, were developed to simulate welding residual stress distribution and deformation in low-alloy high-strength Q345 steel multi-pass butt-welded joint. Then, the hole-drilling method was carried out to measure the welding residual stresses on the surface of the mock-up, while the three-coordinate measuring instrument was used to obtain the out-of-plane deformation distribution of the butt-welded joint. Based on the comparison between simulation results and the measurements, the influence of modeling approach on computing time and prediction accuracy has been clarified in detail.

2 Experimental procedure

As shown in Fig. 1, a butt-welded joint with V groove was fabricated by CO_2 gas arc welding process. The length, width, and thickness of the joint are 300, 300, and 16 mm, respectively. The base metal is low-alloy high-strength steel named Q345, and the filler metal is ER50-2 wire with diameter of 1.2 mm. The chemical compositions of the materials used in the mock-up are summarized in Table 1. The welding method was CO_2 gas arc welding process; welding conditions are shown in Table 2. The specimen was welded by multi-pass welding procedure. The total number of weld pass was five. The sequence of weld pass is schematically illustrated in Fig. 2. During the experiment, the inter-pass temperature was lower than 100 °C.

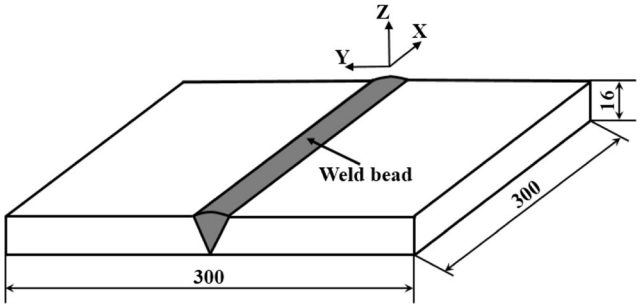

Fig. 1 Dimensions of the specimen (unit: mm)

After welding, the hole-drilling method [18] was used to measure the welding residual stress on the upper surface of the specimen. The measuring locations are shown in Fig. 3. The device used to measure welding residual stress is ASM1.0. The values of the Young's modulus and Poisson's ratio of the Q345 steel were set to be 209 GPa and 0.29 in advance, respectively. Then, the value of residual stress could be automatically calculated through using the released strains measured by the device [19, 20]. The whole experiment process conforms to the standard ASTM E837-08 [19].

At the same time, the out-of-plane deformation of the specimen after welding was measured by a three-coordinate measuring system [21] named ROMER INFINITE 2.0. Deflection distributions of the welded plates were acquired by using the different displacement in *Z*-coordinate before and after welding.

3 Finite element analysis

Based on MSC. Marc code [22], a thermo-elastic–plastic finite element method was proposed to predict welding residual stress and deformation induced by CO_2 gas arc welding in Q345 butt-welded joint with 16-mm thickness. The thermo-mechanical behavior was computed by using a sequentially coupled formulation. Firstly, the welding temperature field is calculated according to the given welding conditions, and then, the temperature history in each node is used as the thermal load in the succeeding mechanical analysis.

In this research, considering geometrical symmetry, half of the model was used for saving the computing time. The dimensions of the 3D models were the same as the experimental

Table 1 Chemical composition of the materials used in the mock-up (wt%)

Material	Composition							
	C	Si	Mn	P	S	Ti	V	Nb
Q345	0.20≤	0.55≤	1.0–1.6	0.045≤	0.045≤	0.02–0.2	0.02–0.15	0.015–0.06
ER50-2	0.09	0.66	1.20	0.016	0.02	–	–	–

Table 2 Welding conditions for each pass

Weld pass number	Welding current (A)	Arc voltage (V)	Welding speed (mm/s)	Net heat input (KJ/mm)
1	105	24.0	1.67	1.51
2	240	28.0	4.62	1.45
3	265	29.0	3.70	2.08
4	265	29.0	3.16	2.43
5	270	29.0	2.86	2.74

specimen. To balance the computing time and the prediction accuracy, finer meshes were designed at the weld zone and its vicinity and their size gradually increased along with the distance from the weld center [20, 23]. To clarify the effect of mesh density in the longitudinal direction on welding residual stress and deformation, two different models were established. In these models, the number of divisions in longitudinal direction is 60 and 20, respectively. In the finite element model with finer mesh, the number of node is 37,515, and the number of element is 33,360. In the finite element model with coarser mesh, the number of node is 12,915, and the number of element is 11,120. The finite element models are shown in Figs. 4 and 5. The element type used in the thermo-mechanical coupled analysis is type 7 (3D brick element) [22].

3.1 Heat source and thermal analysis

During the welding, the element "birth and death" technique was used to simulate the depositing process of the weld bead. In the thermal analysis, transient nonlinear heat transfer analysis was performed by using with appropriate heat source models. The thermal cycle during the welding at each node and the transient temperature distribution in the whole range of model were obtained by the following equation [10]:

$$\rho c \frac{\partial T}{\partial t}(x,y,z,t) = -\nabla \vec{q}(x,y,z,t) + Q(x,y,z,t) \quad (1)$$

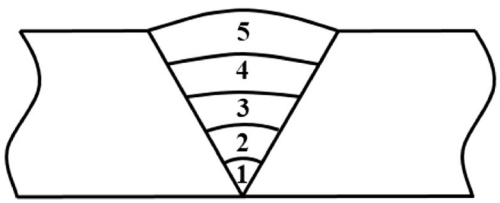

Fig. 2 Weld pass positioning and the welding sequence in cross section

where ρ is the density of the materials (g/mm^3); c is the specific heat capacity (J/(g °C)); T is the current temperature (°C); $\vec{q}$ is the heat flux vector (W/mm^2); Q is the internal heat generation rate (W/mm^3); x, y, and z are the coordinates in the reference system (mm); t is the time; and ∇ is the spatial gradient operator. The nonlinear isotropic Fourier heat flux constitutive equation was employed [10]:

$$\vec{q} = -k\nabla T \quad (2)$$

where k is the temperature-dependent thermal conductivity (J/(mm s °C)).

Generally, the heat source model is considered to be a significant aspect of the welding thermal analysis. In the past decades, a variety of models including cone-shaped volumetric heat source with Gaussian distribution [24] and double-ellipsoidal volumetric heat source [25] are

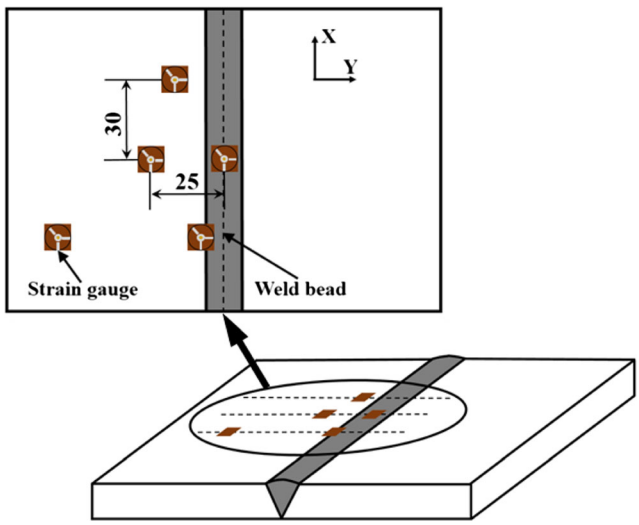

Fig. 3 Locations of strain gauges for residual stress (unit: mm)

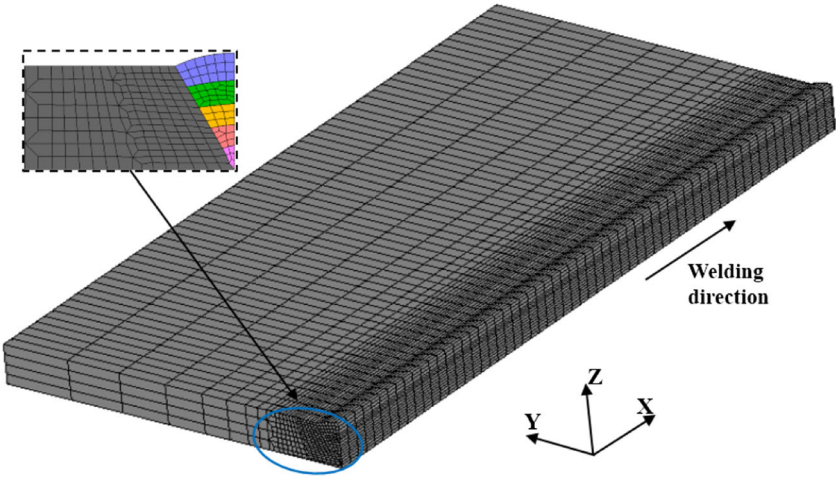

Fig. 4 The finer finite element mesh for the multi-pass butt weld

employed to simulate the welding process. In order to improve the computation efficiency, Sun and Deng et al. [26] developed an instantaneous heat source model. In this study, a double-ellipsoidal volumetric heat source model was employed. Meanwhile, in order to investigate the influence of different modeling approaches on computing time and prediction accuracy of welding residual stress and deformation, an instantaneous heat source model was also employed.

In the double-ellipsoidal volumetric heat source model, the heat input is defined separately over two regions and conveniently expressed by a local coordinate system moving with the heat source. One region is in front of the arc center ($x > 0$), and the other ($x \le 0$) is defined behind the arc. The front half of the source is the quadrant of one ellipsoidal source, and the rear half is the quadrant of another ellipsoid. The schematic of heat flux distribution in double-ellipsoidal volumetric heat source model is shown in Fig. 6.

The power density distribution inside the front quadrant becomes

$$q\left(x^{'},y^{'},z^{'},t\right) = \frac{6\sqrt{3}f_f Q_w}{\pi a_f bc\sqrt{\pi}} e^{-3\left(x'/a_f\right)^2} e^{-3(y'/b)^2} e^{-3(z'/c)^2} \quad (x > 0) \tag{3}$$

Similarly, for the rear quadrant of the source, the power density distribution inside the ellipsoid becomes

$$q\left(x^{'},y^{'},z^{'},t\right) = \frac{6\sqrt{3}f_r Q_w}{\pi a_r bc\sqrt{\pi}} e^{-3(x'/a_r)^2} e^{-3(y'/b)^2} e^{-3(z'/c)^2} (x \le 0) \tag{4}$$

where f_f and f_r are parameters which give the fraction of the heat deposited in the front and rear quadrants, respectively. Note that $f_f + f_r = 2$. In the current study, f_f and f_r are assumed

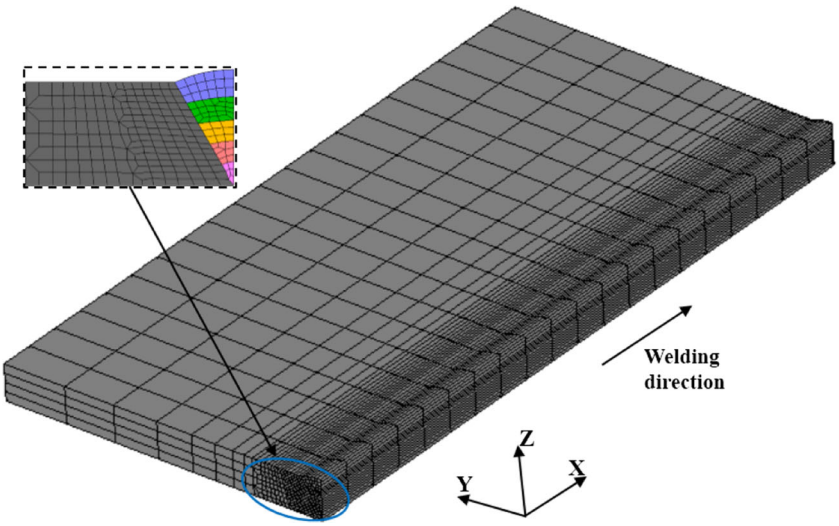

Fig. 5 The coarser finite element mesh for the multi-pass butt weld

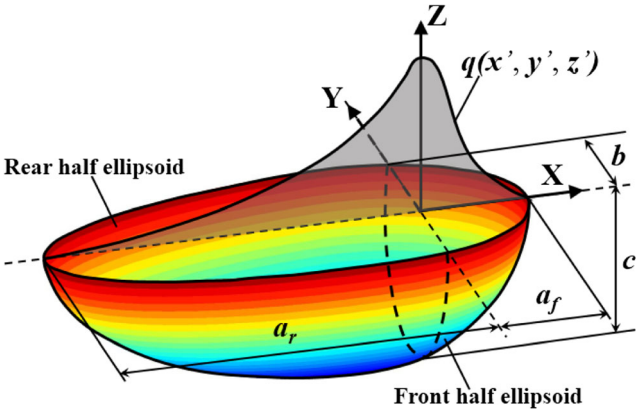

Fig. 6 Double-ellipsoidal volumetric heat source model

to be 0.6 and 1.4, respectively [1]. The ellipsoid axes a_f (or a_r), b, and c are the shape parameters of the double-ellipsoidal volumetric heat source model in x', y', and z' direction, respectively. These shape parameters are adjusted to create a reasonable melted zone according to the welding conditions, and their values are summarized in Table 3. The peak temperature of weld pool is controlled in the range between 1600 and 1800 °C. Q_w is the power of the heat source. It can be calculated according to the welding current, the arc voltage, and the arc efficiency. For CO_2 gas welding process, the arc efficiency (η) is assumed to be 0.8 [27].

In the instantaneous heat source model, there are some characteristics as follows:

- The heat source has a uniform density, and its volume is equal to that of the full weld pass.
- In the finite element model, the cross-sectional area of the heat source is roughly equal to that of weld pass measured by the experiment.
- Heating the whole weld pass and keeping a certain time, the total length of the heat source is equal to that of the weld pass.

For the instantaneous heat source model, the heat input of each weld pass can be calculated by using the welding parameters as shown in Table 2. The heat flux of each weld pass can be obtained by solving the following governing equation:

$$q_i = \frac{\eta U_i I_i L^i}{\upsilon_i t_{hi} V_i} \tag{5}$$

where q_i is the heat flux of the ith weld pass, η is the arc efficient, U_i is the arc voltage, I_i is the welding current, L is the full length of the weld pass, υ_i the welding speed, V_i is the volume of the ith weld pass, and t_{hi} is the total heating time of the ith weld pass. In general, throng several trial computations and comparing the cross-sectional shapes of fusion zone and heat-affected zone with those obtained by moving heat source, the value of t_{hi} can be determined.

Besides considering the heat source model, heat losses due to convention and radiation are also considered in the finite element model. The heat loss caused by convection (q_c) is described as follows [19]:

$$q_c = -h_c(T_s - T_0) \tag{6}$$

where h_c is the heat transfer coefficient, T_s is the surface temperature of the specimen, and T_0 is the ambient temperature which is assumed to be 20 °C. The heat loss due to radiation is considered by using Stefan–Boltzman law [23]:

$$q_r = -\varepsilon\sigma\left\{(T_s + 273)^4 - (T_0 + 273)^4\right\} \tag{7}$$

where ε is the emissivity and σ is the Stefan–Boltzman constant.

In this study, the temperature-dependent thermal physical properties [28] of low-alloy steel (Q345) such as thermal conductivity, density, and specific heat are employed in the thermal simulation as shown in Fig. 7. Furthermore, the thermal effects due to solidification of the weld pool are modeled by taking into

Table 3 Parameters of heat source

Weld pass number	Parameters			
	a_f (mm)	a_r (mm)	b (mm)	c (mm)
1	5	8	4.8	3
2	8	16	6.3	4
3	10	20	6.3	4
4	5	10	13	2.5
5	5	10	17	3.3

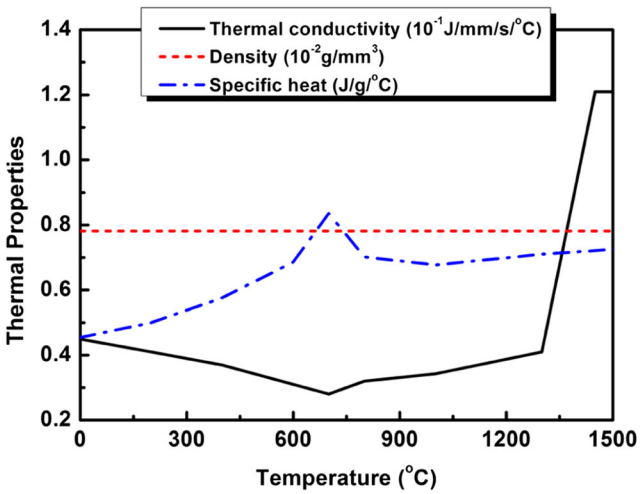

Fig. 7 Temperature-dependent thermal physical properties

account the latent heat for fusion. The value of the latent heat of low-alloy steel is set to be 270 J/g [29] in the finite element model. The liquidus temperature and the solidus temperature are assumed to be 1500 and 1450 °C, respectively.

3.2 Mechanical analysis

In the mechanical analysis, the temperature histories of each node computed by the thermal analysis as the input information. The same finite element mesh was used in the thermal analysis. The boundary conditions of the 3D models which are used to prevent rigid body motion of the 3D models are shown in Fig. 8. In the 3D models, because of the symmetry of the finite element model, the symmetry plane is fixed in *Y*-direction. The point P1 in Fig. 8 is constrained in the *X*-direction and the *Z*-direction, and the point P2 is constrained only in the *Z*-direction. P1 and P2 are the start point and the end point of the centerline in the symmetry plane, respectively. Similar to thermal analysis, the temperature-dependent mechanical properties [28] such as Young's modulus, yield strength, and thermal expansion coefficient were also employed as shown in Fig. 9.

For Q345 steel, because the carbon equivalent is relatively small, it can be inferred that the solid-state phase transformation will have an insignificant influence on the welding residual stress and deformation [30]. In addition, because a relatively large heat input was used to perform the welding, the phase fraction of martensite is very limited in both the fusion zone and heat-affected zone. Based on the above two reasons, the phase change was neglected in the current simulation. In addition, the period with high temperature during the whole thermal cycle was very short, so the creep behavior was also ignored. Therefore, the total strain can be decomposed into three components as follows [31]:

$$\varepsilon_{total} = \varepsilon^{e} + \varepsilon^{p} + \varepsilon^{ts} \tag{8}$$

where ε^{e}, ε^{p}, and ε^{ts} stand for elastic strain, plastic strain, and thermal strain, respectively. Elastic strain is modeled by using the isotropic Hooke's law with temperature-dependent Young's modulus and Poisson's ratio. The thermal strain is calculated by using temperature-dependent coefficient of thermal expansion. For the plastic strain, a rate-independent plastic model is employed with the Von Mises yield surface and

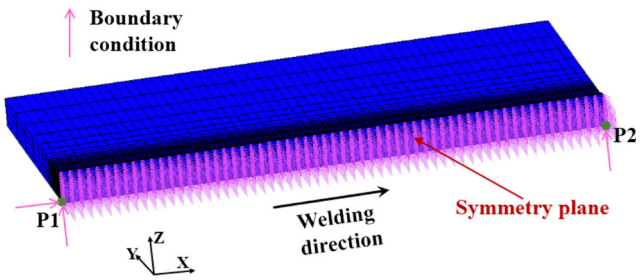

Fig. 8 Mechanical boundary conditions of the 3D model

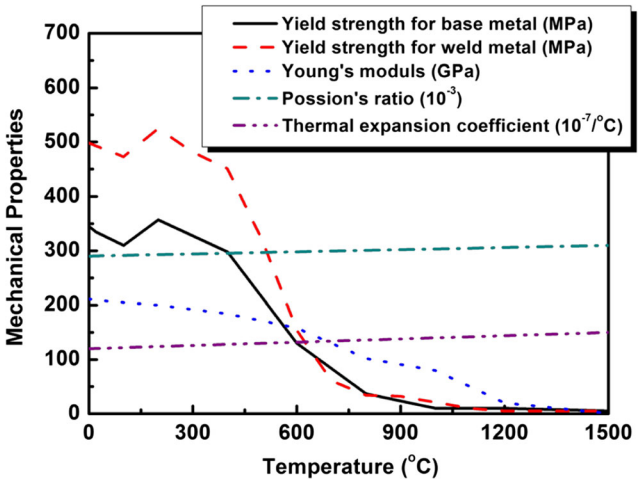

Fig. 9 Temperature-dependent mechanical properties

temperature-dependent mechanical properties. As the effect of work hardening is insignificant in low-carbon steel, it was ignored in this study.

3.3 Simulation cases

In the present study, the analyses of the welding residual stress and deformation were performed on a personal computer with Intel Quad-Core CPU 2.5 GHz. Apart from developing finite element model which accurately simulates the welding residual stress and deformation for multi-pass joints, another emphasis was to investigate an acceptable modeling approach to balance computing time and prediction accuracy. Thus, three cases are performed in the numerical analysis. The simulation cases are showed in Table 4. In case A, a 3D model with finer mesh and a moving heat source is employed to simulate the welding process. In case B, the type of the model is identical to case A, while an instantaneous heat source model is used instead of moving heat source model. In case C, a 3D model with coarser mesh in longitudinal direction and an instantaneous heat source model which is the same as that used in case B is employed.

4 Results and discussions

4.1 Comparison of residual stress

In order to quantitatively compare welding residual stress among three simulation cases, four paths namely line 1, line

Table 4 Simulation cases

Case	Finite element model	Heat source model
Case A	3D model (finer)	Moving heat source
Case B	3D model (finer)	Instantaneous heat source
Case C	3D model (coarse)	Instantaneous heat source

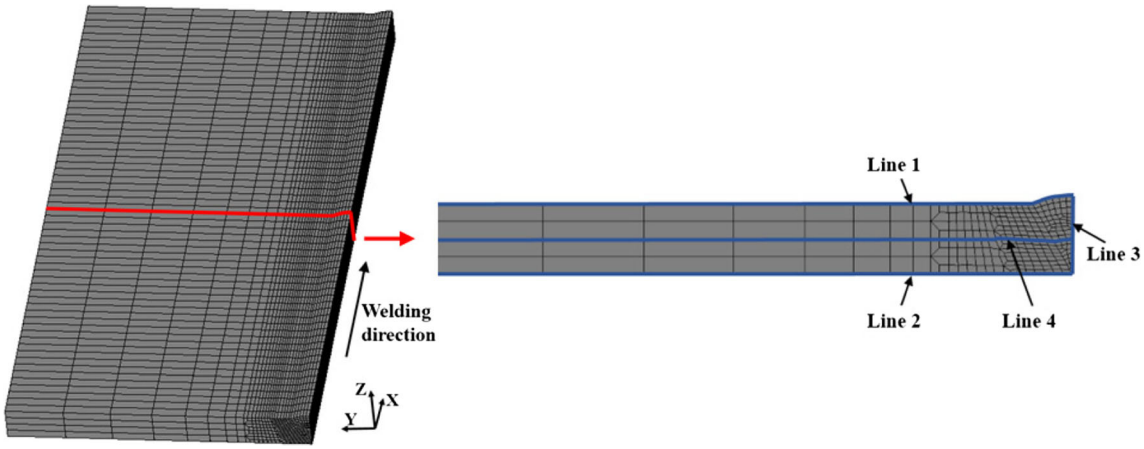

Fig. 10 Middle cross section of the analysis model

2, line 3, and line 4 have been defined in the middle section of fine element model. The four paths are shown in Fig. 10. Line 1 and line 2 are the top and bottom surfaces of the middle cross section, respectively. Line 3 is the central line of the weld, and line 4 is the central line of the middle cross section.

In this section, the simulation results and the measured data are compared. Figure 11a, b shows the longitudinal residual stress distribution and transverse residual stress distribution, respectively. From those figures, it can be observed that the gradient of welding residual stresses is very small along the longitudinal direction in the steady region. Based on these results, the residual stresses measured by experiment can be plotted along the centerline (line 1) of the top surface. Also, it is clear that the maximum longitudinal residual stress appears in the weld zone, while the maximum transverse residual stress occurs in the heat-affected zone.

Figure 12 shows the longitudinal residual stress distributions along line 1. The purple spots represent the experimental measurements obtained by the hole-drilling method; the solid curves, dash curves, and dot curves are the simulated results predicted by case A, case B, and case C, respectively. In this figure, it can be found that the simulated results of the three cases are in very good agreement with the measurements at the weld zone and its vicinity. However, the measurements are larger than the simulated results in the region whose distance from the weld centerline is larger than 15 mm. This difference is caused by the initial residual stresses introduced by the manufacturing process before welding [32]. Because the weld zone and its vicinity underwent a thermal cycle with high peak temperature during welding process, the initial residual stresses in this region were completely canceled by welding. Therefore, the initial residual stress has no influence on the final residual stress after welding. In contrast, the initial residual stresses in the region which are far away from the weld zone were hardly influenced by welding process because the peak temperatures were not high enough. Comparing the simulated results, it can be seen that the shapes of longitudinal residual stress distribution of three cases are much similar. Carefully observing this figure, one can find that the longitudinal tensile residual stresses within the region of 15 mm $\leq Y \leq$ 30 mm in case A are higher than those in case B and case C. It is interesting that there is nearly no difference between case B and case C. The peak tensile stresses of case A, case B, and case C are 489, 493, and 493 MPa, respectively. These values are very close to the yield strength of weld metal (487 MPa) at room temperature.

Figure 13 shows the transverse residual stress distributions along line 1 predicted by these three simulation cases. Meanwhile, the corresponding measured data are plotted in the same figure. From this figure, one can know that although

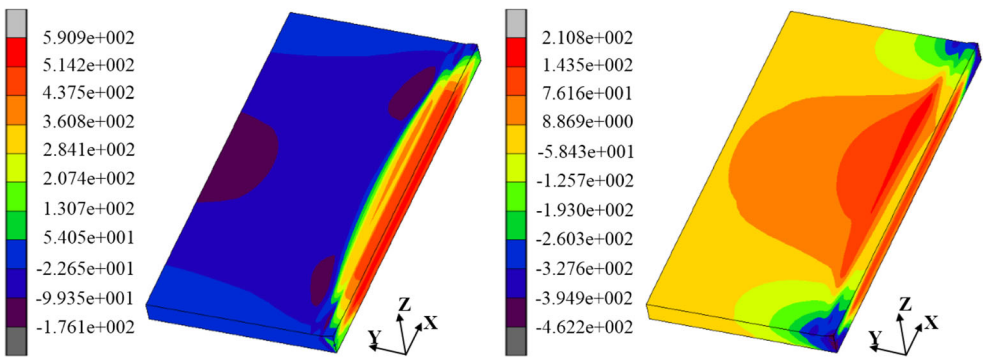

Fig. 11 Residual stress distributions. **a** Longitudinal residual stress distribution. **b** Transverse residual stress distribution

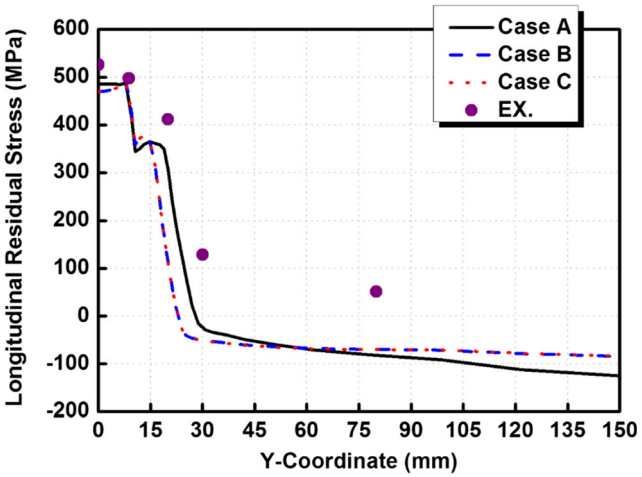

Fig. 12 Longitudinal residual stress distribution along line 1

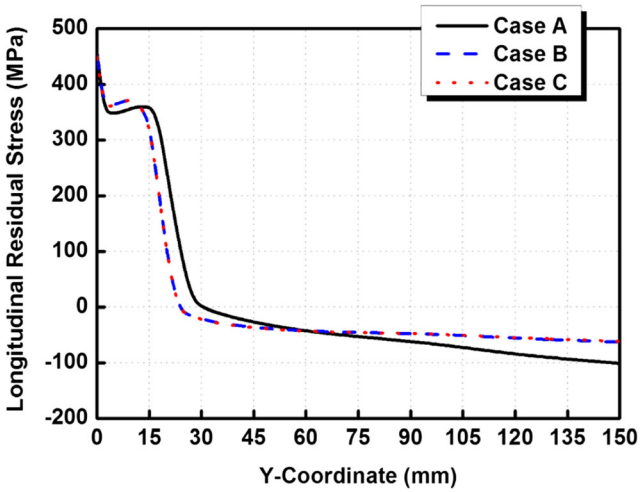

Fig. 14 Longitudinal residual stress distribution along line 2

the shape of transverse residual stress distribution measured by experiment is roughly similar to those predicted by finite element model, the measured data are slightly larger than the simulated results. Comparing these three simulation cases, it can be found that case B and case C almost have the same distribution shape, while there are some differences between case A and case C. The maximum value of both case B and case C is 200 MPa, and this is larger than the peak value of case A, which is 150 MPa.

Both Figs. 12 and 13 suggest that the residual stress distributions along line 1 are slightly affected by the heat source model, while it seems not sensitive to the mesh density in longitudinal direction.

Figures 14 and 15 compare the distributions of longitudinal and transverse residual stress along line 2, respectively. Figure 14 tells us that the numerical results of the three cases are generally similar in the whole range. Carefully comparing, it is clear that the region with high longitudinal tensile stress in case A is slightly wider than those in case B and case C. One can also obverse that there is a difference between case A and case B within the region of 15 mm $\leq Y \leq$ 30 mm, while there is no difference between case B and case C.

Figure 15 is similar to Fig. 14; there are some differences between case A and case B, but there is no difference between case B and case C.

Figures 16 and 17 show the distribution of longitudinal and transverse residual stress along line 3, respectively. From Fig. 16, one can know that case A is slightly different from case B and case C, while the difference between case B and case C is insignificant. The maximum value of longitudinal residual stress of both case B and case C is 560 MPa, while that of case A is 550 MPa. This peak value is larger than the yield strength of the weld metal at room temperature. Base on the above comparison, it can be concluded that the longitudinal residual stress is not sensitive to heat source model and mesh density in welding direction.

From Fig. 17, it can be found that transverse residual stresses are much smaller than the longitudinal residual stresses. Similar to Fig. 16, there are some differences

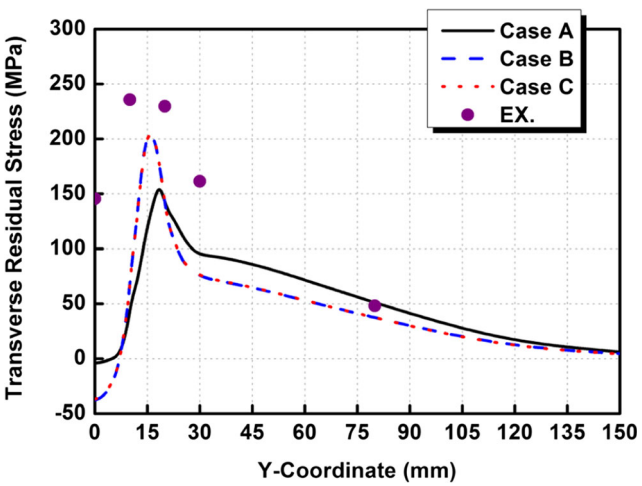

Fig. 13 Transverse residual stress distribution along line 1

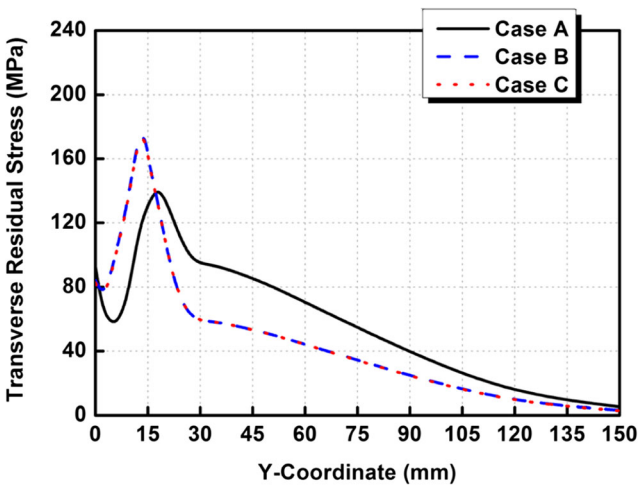

Fig. 15 Transverse residual stress distribution along line 2

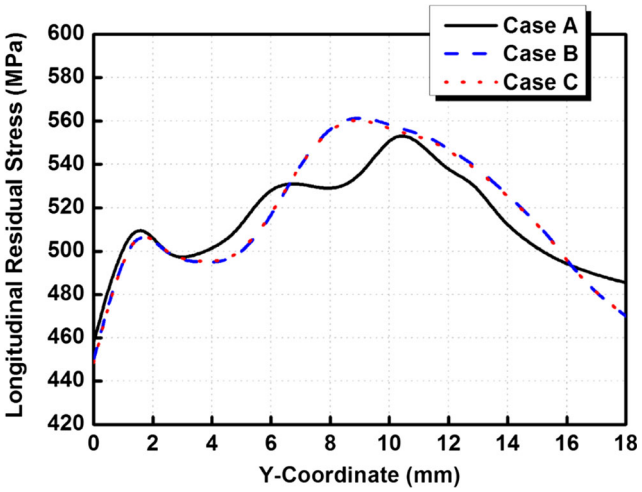

Fig. 16 Longitudinal residual stress distribution along line 3

between case A and case B, while there is no difference between case B and case C. This figure indicates that the heat source model can affect the transverse residual stress to some extent, while mesh density in welding direction has a very limited influence.

Figures 18 and 19 show the longitudinal residual stress distributions and transverse residual stress distributions simulated by those three cases along the welding line on the top surface, respectively. One can know that the shape of residual stress computed by case A, case B, and case C is very similar, and there is no difference between case B and case C within the region of 50 mm < X < 250 mm. In addition, the longitudinal and transverse residual stress distributions predicted by both case B and case C have a symmetric shape with respect to the line with X = 150 mm, while those computed by case A are asymmetric. As shown in Figs. 18 and 19, both the maximum longitudinal stress and the peak transverse stress of case A

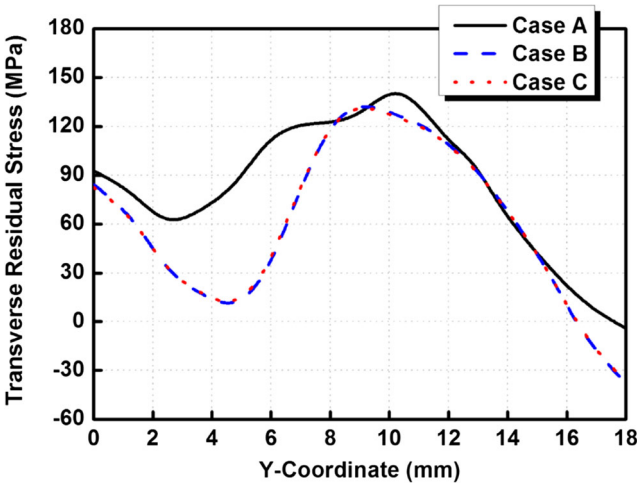

Fig. 17 Transverse residual stress distribution along line 3

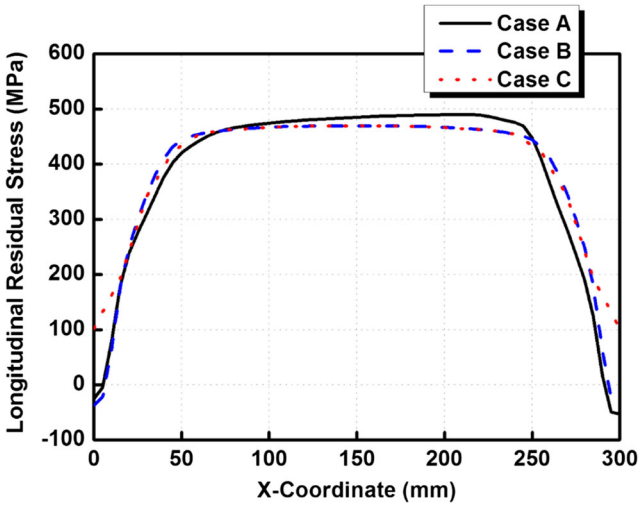

Fig. 18 Longitudinal residual stress distribution along the welding line on the top surface

appear at the location with X = 220 mm. In Fig. 18, the maximum value of longitudinal residual stress simulated by case A is about 500 MPa, while the peak values of longitudinal residual stress simulated by case B and case C are approximately 480 MPa. These are very close to the yield strength of weld metal (487 MPa) at the room temperature.

Through comparing the residual stress distributions among case A, case B, and case C, it can be observed that even though case A can provide a more detailed information on residual stress distribution, the differences among three cases are not significant. This means that case C with instantaneous heat source model and coarse mesh density in welding direction can provide an acceptable simulation result of welding residual stress.

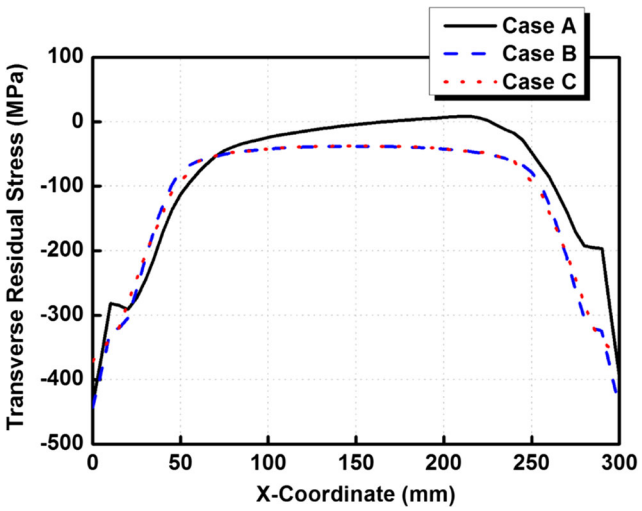

Fig. 19 Transverse residual stress distribution along the welding line on the top surface

4.2 Comparison of welding deformation

4.2.1 Transverse shrinkage

Figure 20 compares the transverse shrinkage (*Y*-displacement) distributions on the middle cross section of the plate simulated by case A, case B, and case C. From this figure, it is clear that the transverse shrinkage distributions have a large gradient at the weld zone and its vicinity. It also can be found that the maximum absolute values of transverse shrinkage simulated by those three cases are about 1.12, 0.27, and 0.28 mm, respectively. Furthermore, it can be seen that transverse shrinkage distributions through thickness in these three cases are uniform. The top surface has the largest shrinkage, while the bottom has the smallest one.

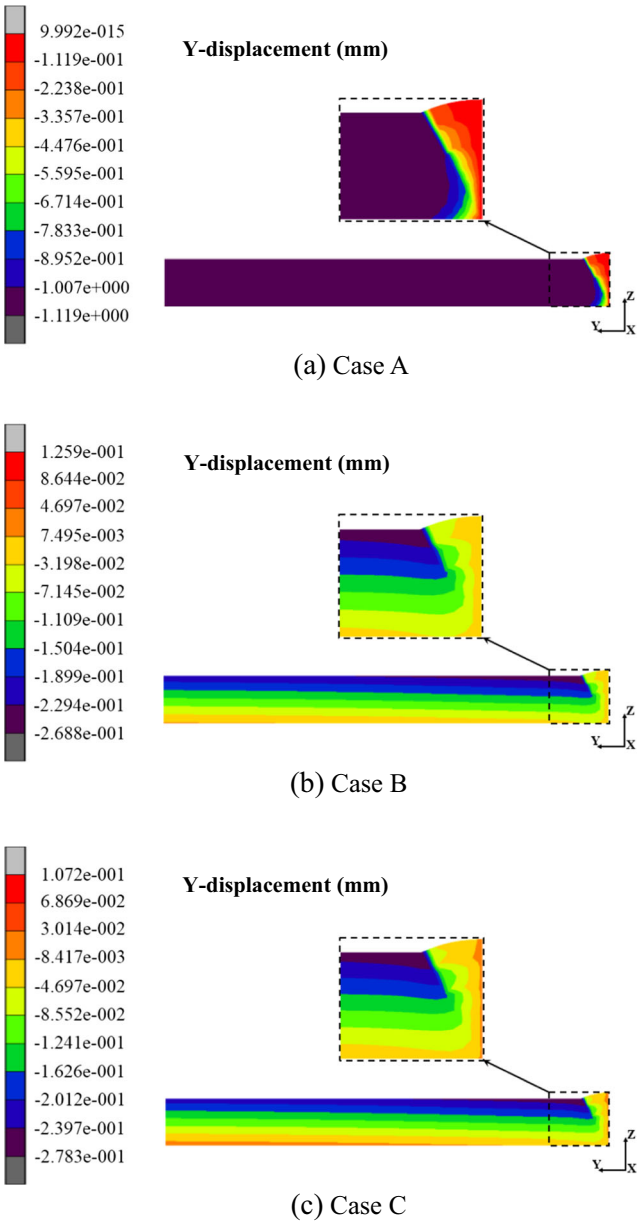

Fig. 20 Transverse shrinkage distributions on the mid-section computed by three simulation cases. **a** Case A. **b** Case B. **c** Case C

Figure 21 compares the transverse shrinkage deformation along line 4. In this figure, one can find that the absolute value of transverse shrinkage increases rapidly at the weld zone and its vicinity, and then, the curves converge to stable value. In addition, the absolute values of case A are much larger than the other two cases. This is because when case B and case C employed the instantaneous heat source model, the materials along the welding line experienced similar thermal cycles at the same time. It can result in a substantial reduction of the restraint intensity in transverse direction. Because a moving heat source model was used in case A, the restraint intensity in transverse direction is larger than case B and case C. During heating, a large compressive plastic strain in transverse direction produced in case A, while relatively small plastic strain generated in case B and case C because of the weaker constraint.

4.2.2 Out-of-plane deformation

Figure 22 compares the deflection distributions along line 1 computed by case A, case B, and case C, and the corresponding measurements are also plotted in the same figure. From the figure, it can be found that the numerical results predicted by case A match the experimental measurements well both in shape and in magnitude, whereas the simulation results of case B and case C are significantly smaller than the measured data. This figure also tells us that the simulation result of case B is roughly the same as that of case C. Comparing these three cases, it can be observed that the maximum deflection of case A is approximately 4.8 mm, and the maximum deflections in case B and case C are about 2.3 mm. Thus, the out-of-plane deformation predicted by moving heat source model is almost twice as large as that simulated by instantaneous heat source

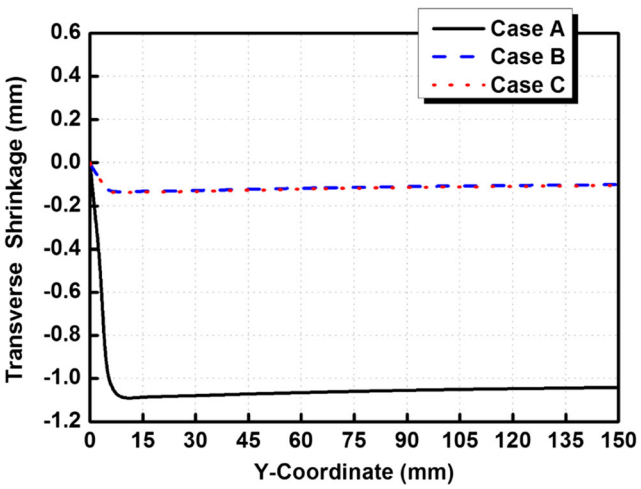

Fig. 21 Transverse shrinkage deformation along line 4

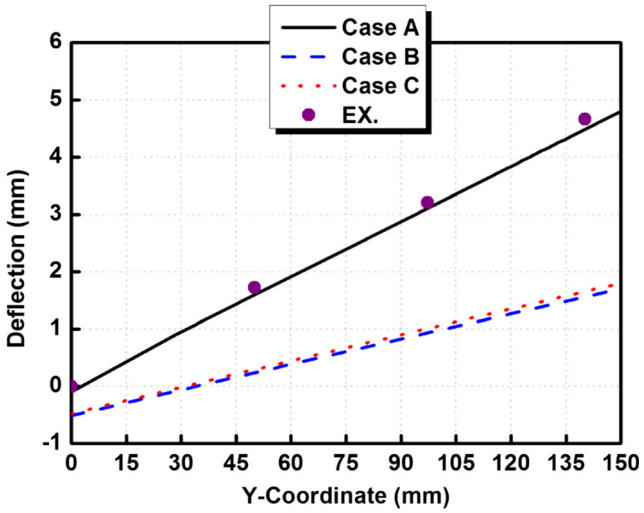

Fig. 22 Comparison of deflection distributions along line 1

model. Therefore, to obtain an accurate prediction of out-of-plane deformation, a moving heat source model is recommended to simulate the thermo-mechanical behavior for the butt-welded joint.

4.3 Comparison of computing time

Based on case A, the relative computing time percentages of case B and case C are shown in Fig. 23. This figure indicates that the computing time of a moving heat source model with a finer mesh (case A) is twice as long as that of an instantaneous heat source model with a finer mesh (case B) and three times longer than that of an instantaneous heat source model with a coarser mesh (case C). This information suggests that both heat source model and mesh density can significantly influence the total computing time.

Although case B and case C cannot provide a reasonable prediction of welding deformation including transverse shrinkage and deflection, these two cases can estimate welding residual stress with an acceptable accuracy. If we only pay attention to welding residual stress, the modeling approach such as case C with an instantaneous heat source and a coarser mesh density in longitudinal direction may be a good choice. Such modeling approach can largely save computing time, and this is very meaningful for the thick-plate multi-pass welded joints.

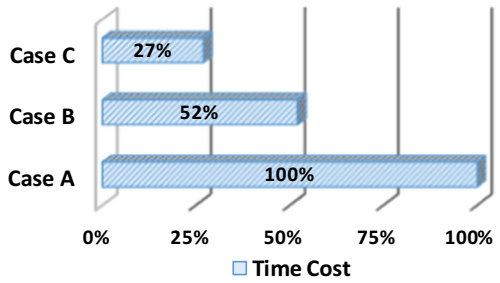

Fig. 23 Comparison of computing time

5 Conclusions

In this study, three 3D finite element models with different heat source model and mesh density were developed to analyze residual stress distribution and deformation in a low-alloy high-strength Q345 steel multi-pass butt joint. The prediction accuracy and computing time were compared among these three models. Through comparing the simulated results and the experimental data, the following conclusions can be drawn.

1. The distribution and value of residual stresses calculated by the instantaneous heat source model and the moving heat source model not only are nearly the same but also both match well with measurements. It indicates that the heat source model has insignificant influence on welding residual stress distribution in a multi-pass butt-welded joint.

2. The welding deformation predicted by the moving heat source model matches the experimental measurements, while the instantaneous heat source model provided a poor prediction of welding deformation.

3. When the instantaneous heat source model is used to simulate welding residual stress, the mesh density (in the range between 5 and 15 mm) in the longitudinal direction seems to have a limited influence on the final calculated results both in residual stress and deformation in the current model.

4. Through comparing among these three cases, it is conservatively stressed that the model with instantaneous heat source and coarse mesh density can largely save the computing time. If we only focus on the final residual stress distribution of a multi-pass joint, this modeling approach may be a good choice because of a shorter computing time and a relatively high accuracy. It is very meaningful for practical thick-plate welded joint with a large number of weld pass.

Acknowledgements The authors gratefully acknowledge the financial support by the National Nature Science Foundation of China (Project No. 51275544).

References

1. Deng D, Murakawa H (2006) Numerical simulation of temperature field and residual stress in multi-pass welds in stainless steel pipe and comparison with experimental measurements. Comput Mater Sci 37(3):269–277
2. Ueda Y (2012) Welding deformation and residual stresses prevention. Elsevier LTD, Oxford
3. Chen BQ, Soares CG (2016) Numerical and experimental investigation on the weld-induced deformation and residual stress in stiffened plates with brackets. Int J Adv Manuf Technol 86:2723–2733

4. Kiyoshima S, Deng D, Ogawa K, Yanagida N, Saito K (2009) Influences of heat source model on welding residual stress and distortion in a multi-pass J-groove joint. Comput Mater Sci 46(4): 987–995
5. Barsoum Z, Barsoum I (2009) Residual stress effects on fatigue life of welded structures using LEFM. Eng Fail Anal 16(1):449–467
6. Lindgren LE (2006) Numerical modelling of welding. Comput Method Appl M 195(48–49):6710–6736
7. Mackerle J (1996) Finite element analysis and simulation of welding: a bibliography (1976-1996). Model Simul Mater Sci 4(5):501–533
8. Barsoum Z, Lundbäck A (2009) Simplified FE welding simulation of fillet welds—3D effects on the formation residual stresses. Eng Fail Anal 16(7):2281–2289
9. Guirao J, Rodríguez E, Bayón A, Jones L (2009) Use of a new methodology for prediction of weld distortion and residual stresses using FE simulation applied to ITER vacuum vessel manufacture. Fusion Eng Des 84(12):2187–2196
10. Nezamdost MR, Esfahani MRN, Hashemi SH, Mirbozorgi SA (2016) Investigation of temperature and residual stresses field of submerged arc welding by finite element method and experiments. Int J Adv Manuf Technol 87:615–624
11. Cai ZP, Zhao HY, Wu S, Lu AL, Shi QY (2001) Model of string heat source in welding numerical simulation. Chin J Mech Eng 37(4):25–28 **43**
12. Hong JK, Tsai CL, Dong P (1998) Assessment of numerical procedures for residual stress analysis of multipass welds. Welding J-New York 77(9):372–382
13. Nishikawa H, Serizawa H, Murakawa H (2007) Actual application of FEM to analysis of large scale mechanical problems in welding. Sci Technol Weld Join 12(12):147–152
14. Murakawa H, Oda I, Ito S, Serizawa H, Shibahara M, Nishikawa H (2005) Iterative substructure method for fast computation of thermal elastic plastic welding problems. J Kansai Soc Naval Arch Jap 243:67–70
15. Deng D, Kiyoshima S (2010) Numerical simulation of welding residual stresses in a multi-pass butt-welded joint of austenitic stainless steel using variable length heat source. Acta Metall Sin 46(2): 195–200
16. Barsoum Z, Bhatti AA, Balawi S (2015) Computational weld mechanics—towards a simplified and cost effective approach for large welded structures. Procedia Eng 114:62–69
17. Ma N (2016) An accelerated explicit method with GPU parallel computing for thermal stress and welding deformation of large structure models. Int J Adv Manuf Technol 87:2195–2211
18. Rendler NJ, Vigness I (1966) Hole-drilling strain-gage method of measuring residual stresses. Exp Mech 6(12):577–586
19. Deng D, Zhou Y, Bi T, Liu X (2013) Experimental and numerical investigations of welding distortion induced by CO_2 gas arc welding in thin-plate bead-on joints. Mater Des 52(24):720–729
20. Ye Y, Cai J, Jiang X, Dai D, Deng D (2015) Influence of groove type on welding-induced residual stress, deformation and width of sensitization region in a SUS304 steel butt welded joint. Adv Eng Softw 86(C):39–48
21. Yan DY, Wu AP, Silvanus J, Shi QY (2011) Predicting residual distortion of aluminum alloy stiffened sheet after friction stir welding by numerical simulation. Mater Des 32(4):2284–2291
22. MSC. Software Corporation (2010) Theory and user information. Santa Ana, CA, USA
23. Sun J, Liu X, Tong Y, Deng D (2014) A comparative study on welding temperature fields, residual stress distributions and deformations induced by laser beam welding and CO_2 gas arc welding. Mater Des 63(2):519–530
24. Lundbäck A, Runnemalm H (2013) Validation of three-dimensional finite element model for electron beam welding of Inconel 718. Sci Technol Weld Join 10(6):717–724
25. Goldak J, Chakravarti A, Bibby M (1984) A new finite element model for welding heat sources. Metall Mater Trans B Process Metall Mater Process Sci 15(2):299–305
26. Sun J, Deng D, Ye Y, He J, Xia L (2016) Numerical simulation of welding residual stress in a multi-pass T-joint of thick Q390 high strength steel plate using instantaneous heat source. Trans Chin Weld Inst 37(7):31–34 **38**
27. Radaj DIHD (1992) Heat effects of welding. Springer, Berlin Heidelberg
28. Cai J, Sun J, Xia L, Deng D (2015) Prediction on welding residual stress and deformation in Q345 steel butt-welded joints. Trans Chin Weld Inst 36(11):61–64 **68**
29. Zhang W, Elmer JW, Debroy T (2002) Modeling and real time mapping of phases during GTA welding of 1005 steel. Mater Sci Eng A 333(1–2):320–335
30. Deng D (2009) FEM prediction of welding residual stress and distortion in carbon steel considering phase transformation effects. Mater Des 30(2):359–366
31. Chen BQ, Soares CG (2016) Effect of welding sequence on temperature distribution, distortions, and residual stress on stiffened plates. Int J Adv Manuf Technol 86:3145–3156
32. Deng D, Kiyoshima S (2010) Numerical simulation of residual stresses induced by laser beam welding in a SUS316 stainless steel pipe with considering initial residual stress influences. Nucl Eng Des 240(4):688–696